Journal of Nuclear Materials 399 (2010) 208–211

Contents lists available at ScienceDirect

Journal of Nuclear Materials

journal homepage: www.elsevier.com/locate/jnucmat

Microstructural characterization of ZrO_2 layers formed during the transition to breakaway oxidation

Dong Jun Park [a,*], Jeong Yong Park [a], Yong Hwan Jeong [a], Jeong Yong Lee [b]

[a] Nuclear Convergence Technology Division, Korea Atomic Energy Research Institute, 1045 Daedeok-daero, Yuseong-gu, Daejeon 305-353, Republic of Korea
[b] Department of Materials Science and Engineering, Korea Advanced Institute of Science and Technology, 373-1 Guseong-dong, Yuseong-gu, Daejeon 305-701, Republic of Korea

ARTICLE INFO

Article history:
Received 21 September 2009
Accepted 29 January 2010

ABSTRACT

In order to characterize the microstructure of oxide layers formed on Zircaloy-4 tubes during the breakaway transition, oxidation tests in a flowing steam environment were performed at 1000 °C with a different oxidation time. It was found that breakaway oxidation occurred after the oxidation time of 3000 s, and zirconium dioxide layers existed in two mixed crystallographic forms of the tetragonal and monoclinic phase in all samples. The zirconium oxide layers showed enhanced crystallinity, increase in grain size, and fine pores at the grain boundary after breakaway oxidation. We found that the initiation of breakaway oxidation instability originated from these microstructural changes.

1. Introduction

Zirconium (Zr) based alloys have been extensively studied due to their fairly good resistance to corrosion from water at elevated temperatures and a very low absorption cross-section of thermal neutrons, and also their potential use in the nuclear industry. The main application is thin-walled tubes used to clad radioactive fuel in boiling water reactors (BWRs). The most commonly used alloy is Zircaloy-4, which is Zr primarily alloyed with tin and iron.

In view of the fact that the fuel cladding have to maintain its fuel integrity in a postulated design-based accident as well as during a normal operation, a loss of coolant accident (LOCA) is considered as one of the most important postulated design-basis accidents in a light water reactor (LWR). When a small break LOCA occurs, the temperature of the fuel system rises rapidly and the cladding undergoes an oxidation for relatively longer periods of time at environment of the mixture of water and steam until it is quenched by emergency core cooling water [1]. As a result, significant oxidation takes place on the surface of the cladding tube during the LOCA, and prolonged exposure to steam can cause breakaway oxidation phenomenon which is described by linear oxidation kinetics with a sudden increase in the oxidation rate which follows initial parabolic regimes [2]. This phenomenon could severely promote embrittlement of the cladding, therefore it is very important to explain precisely why this breakaway oxidation takes place during the LOCA for safety analysis. However, no mechanism has been generally accepted for the explanation of pre- to post-breakaway kinetics and its actual process is still a matter of controversy, although extensive investigations have been carried out [3–8]. Furthermore, most investigations of them were performed at a lower temperature than a real LOCA condition. However, high temperature oxidation test should be conducted for simulating almost real accident condition and for understanding what happens to oxide layer formed on cladding during actual LOCA. Few studies have been published on the mechanisms of breakaway oxidation in actual LOCA conditions, but microstructural analysis studies were carried out with just low magnification using optical microscopy (OM), scanning electron microscopy (SEM), transmission electron microscopy (TEM), etc.

In this study, we attempted to synthesize the microstructure and atomic arrangement of the oxide layer formed on Zircaloy-4 tube at a temperature of 1000 °C by using a high resolution TEM (HRTEM). As a result, we observed flat grain boundaries (GBs) and micro-pores between the enlarged grains in post-breakaway oxide layer. We propose a mechanism to explain how these microstructural changes play a crucial role in transition to the breakaway and contribute to the enhanced oxidation rate.

2. Experimental procedure

A Zircaloy-4 tube which has a 200 mm length was used in this study and specimen temperature was measured by a pyrometer. Direct heating by an ohmic resistance with feedback between the pyrometer and the power supply enabled the specimen to heat up to temperatures of 1000 °C. Then the specimen was oxidized in a flowing steam with different exposure times in the range of 300–4000 s. Finally, the specimen was cooled at an intermediate

* Corresponding author. Tel.: +82 42 868 4849; fax: +82 42 862 0432.
E-mail address: pdj@kaeri.re.kr (D.J. Park).

0022-3115/$ - see front matter © 2010 Elsevier B.V. All rights reserved.
doi:10.1016/j.jnucmat.2010.01.021

temperature of 700 °C for 200 s after oxidation and then quenched because the apparent temperatures do not abruptly drop at first until a sufficient amount of coolant is flooded into the core. All the data and procedures were collected and controlled by a main computer. The detailed illustration and description of experimental procedures of the simulated LOCA facility can be founded in previous work already reported by our group [9]. The metallographic study and cross-sectional morphology of the oxide layer was investigated by OM with a polarized filter, and the HRTEM (JEM 3010) operated at 300 kV. TEM samples sectioned from the oxidized tube were polished mechanically and then argon ion thinned for electron transparency.

3. Results and discussion

Fig. 1 shows the morphology of the ZrO_2 layers formed on the Zr tube with different oxidation times of 300 s (sample A), 2000 s (sample B), 3000 s (sample C), and 4000 s (sample D). In previous result reported by our group, similar oxidation tests were carried out at 1000 °C. At that time, the in situ measuring method was used to determine the weight gain during an oxidation and the breakaway oxidation of the Zircaloy-4 alloy occurred after an exposure for about 3100 s. It can be found that the breakaway oxidation time of the Zircaloy-4 alloys was almost the same from the repeatedly performed tests for the various exposure times [10]. This is the reason why these test times from 1000 s to 4000 s were selected, although experimental instrument used for oxidation in this study is not a same one. Sample A showed a uniform oxide layer with a mean thickness of 41.7 μm. Thickness of the oxide layer increased slightly up to an oxidation time of 3000 s, but sample D showed a sudden increase in the thickness of the oxide layer due to breakaway oxidation. The lateral crack parallel to the interface between oxide and metal (see arrow in Fig. 1d) was formed during the transition to breakaway oxidation. Based on results of the previous report [4], it seems likely that the oxide layer below the arrow is the black hypostoichiometric oxide (anion-deficient) and the upper one is the white (or grey) stoichiometric oxide. Oxygen-stabilized alpha phase was formed beneath the oxide layer in all samples because of the oxygen diffusion along the cladding thickness and excess of oxygen solubility limit in prior beta region. The thickness of alpha layer increased as the oxidation time increased, as shown in Fig. 1a–d.

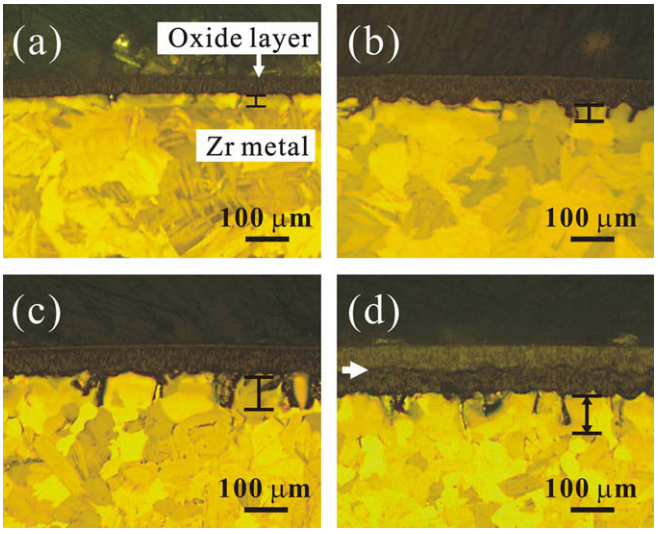

Fig. 1. Optical metallographs of outer surface oxide layers oxidized at 1000 °C with different oxidation times: (a) 300 s, (b) 2000 s, (c) 3000 s, and (d) 4000 s.

Cross-sectional bright-field TEM images of the oxide layer from samples A and D are shown in Fig. 2a and b. While sample A showed high density columns vertically aligned with round tips, enlarged grains having fine pores in GBs (see arrows and inset of Fig. 2b) were observed in sample D. Selected area diffraction patterns (SADPs) obtained from both samples indicate that oxide layers of sample A and D are composed of two mixed crystallographic forms of the tetragonal and monoclinic phase. However, it is not absolutely clear due to very similar interplanar spacing distances of several planes of the two crystallographic phases, such as the (2 0 0) plane of monoclinic ZrO_2 and the (1 1 0) plane of tetragonal ZrO_2. The SADP was converted from an initial ring pattern to a spotty one. These results reveal that crystallinity and the size of grains in the oxide layer changed during breakaway oxidation, i.e., small grains having a random distribution in crystalline orientation changed to large grains with high crystallinity and the same crystalline orientation due to a longer oxidation time at a high temperature.

HRTEM analysis was performed to characterize the detailed microstructural properties of the oxide layer in sample A. A representative HRTEM image was taken from middle region of oxide layer. As shown in Fig. 3, the boundary shape between columns was unclear and uneven. Moreover, crystalline orientations in the same column show a slight difference depending on the location. For analyzing the crystalline structure, fast-Fourier-transformed (FFT) diffraction patterns were obtained from each region labeled as A, B, and C. Based on distances and angles between spots determined from the FFT image, the FFT diffraction patterns from regions A, B, and C are indexed and determined to be the diffraction patterns for the tetragonal structure with the $[\bar{1}\,1\,1]$ zone axis (ZA), the monoclinic structure with the $[\bar{1}\,1\,0]$ ZA, and the tetragonal structure with the $[\bar{1}\,1\,0]$ ZA, respectively. From these results and the SADP of sample A in Fig. 2, it is concluded that the oxide layer of sample A is composed of two mixed crystallographic forms of the tetragonal and monoclinic phase.

The oxide layer of sample D was also characterized by HRTEM. The micrograph in Fig. 4 was obtained from the oxide layer below arrow in Fig. 1d. In contrast to the result of sample A (Fig. 3), the oxide layer of sample D showed larger grains with very flat GB, and crystalline orientation in each grain was completely the same. This change in the grain morphology means that grain growth occurs continuously as the oxidation time increases. The driving force for the grain growth and flat boundaries is the excess boundary energy of grains [11] because reduced boundaries due to larger grains with a flat boundary are more energetically favored than a smaller one with a rough boundary. Fast-Fourier-transformed (FFT) diffraction patterns obtained from each region labeled as A and B were indexed, as shown in Fig. 4. Although it revealed that both grains in Fig. 4 were monoclinic structure with the [1 1 0] ZA and the $[0\,\bar{1}\,1]$ ZA, a tetragonal structure was also observed in the HR TEM result obtained from another region (not shown here). Considering the SADP in Fig. 2, therefore, we know that the oxide layer of sample D is also composed of two mixed crystallographic forms of the tetragonal and monoclinic phase. These results mean that oxide layers of pre- and post-breakaway oxidation do not differ in crystalline structure. Although several investigators [12,13] have suggested that the transition at breakaway is probably caused by a change in the oxide structure from cubic or tetragonal to monoclinic, our results reveal that no effect of such a change would be expected to give rise to the breakaway oxidation.

From the results mentioned above (Figs. 1–4), we conclude in partial consistence with Keys et al. [14] that the breakaway oxidation phenomena is associated with the change of non-stoichiometric (anion-deficient) and protective black oxide into stoichiometric and non-protective white (or grey) oxide. This change accompanies a decrease in the plasticity of the oxide layer and

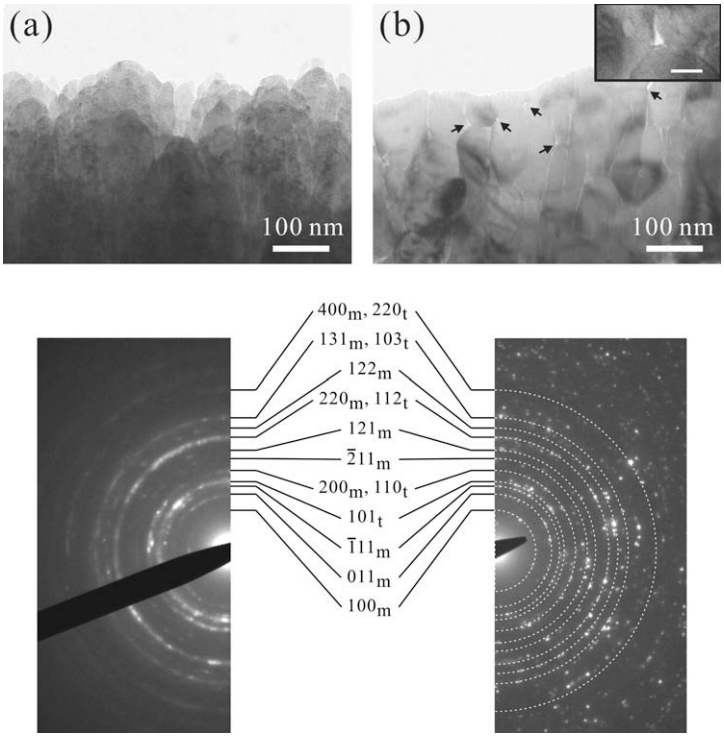

Fig. 2. Cross-sectional bright-field TEM micrographs obtained from the oxide layers of (a) sample A and (b) D. The inset of (b) shows the enlarged TEM image of a grain boundary containing a micro-pore, and the scale bar denotes 20 nm. Corresponding SADPs of the oxide layer are shown in the bottom of each BF TEM image.

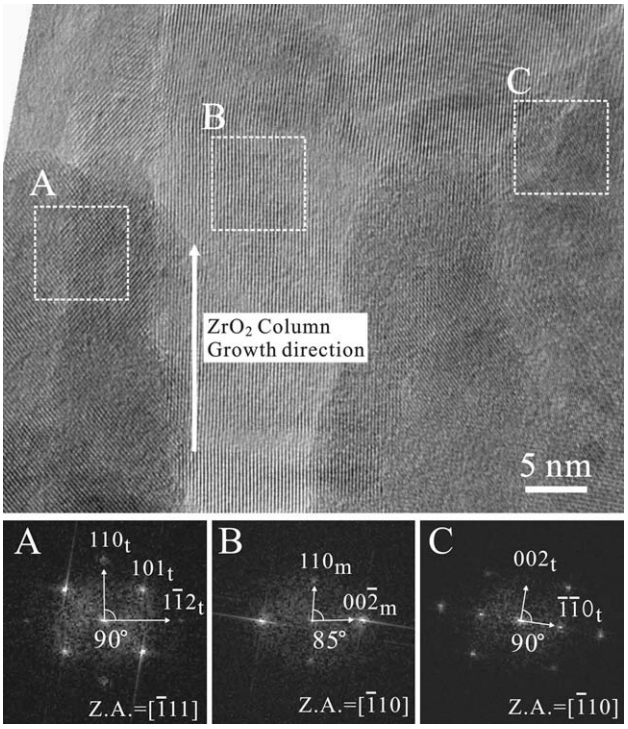

Fig. 3. Cross-sectional HR TEM image taken from the oxide layer of sample A. Fast-Fourier-transformed patterns corresponding to marked square regions of A, B, and C are shown in the bottom.

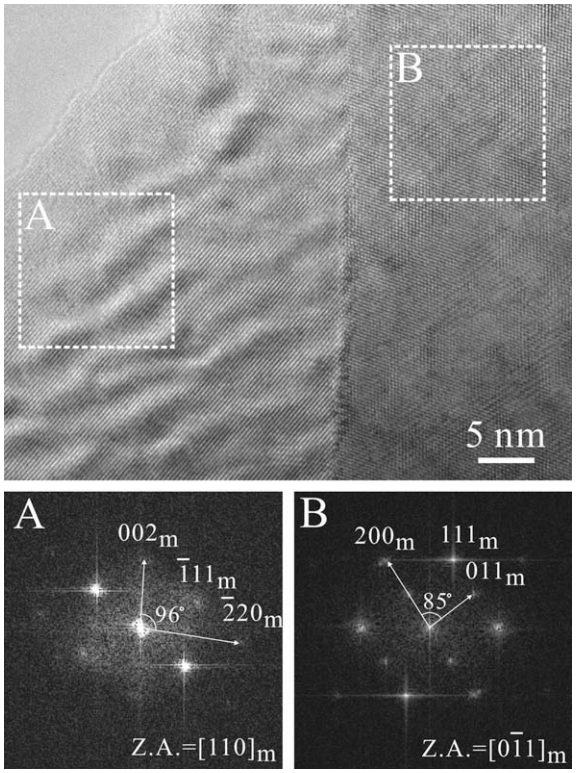

Fig. 4. Cross-sectional HR TEM micrograph obtained from the oxide layer of sample D. The images on the bottom show corresponding fast-Fourier-transformed diffraction patterns for regions A and B, respectively.

leads to cracks in the outer stoichiometric region and a mechanical breakdown under the growth stress originating from a high value (1.56) for the Pilling–Bedworth ratio [4]. Consequently, this resultant stoichiometric layer of oxide is separated from the underlying non-stoichiometric layer. The protective barrier for oxidation is then greatly reduced and the oxidation rate is increased suddenly. However, Keys et al. did not offer a clear explanation for enhanced

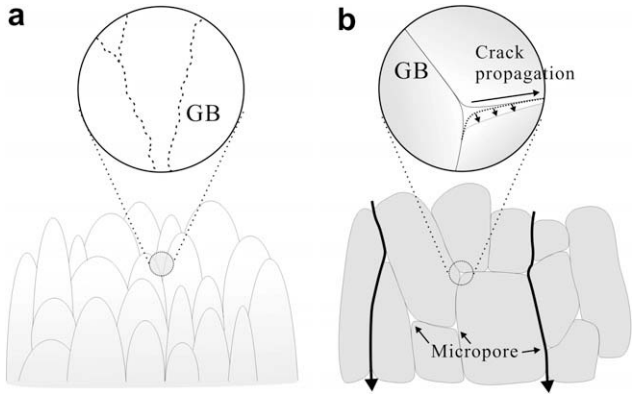

Fig. 5. Schematic diagrams of (a) the oxide layer formed at pre-breakaway kinetics, and (b) the oxide layer formed during the transition to breakaway oxidation.

oxygen diffusivity in the stoichiometric region and the origin of mechanical cracks. In this process of breakaway transition, we found that initiation of the stoichiometric change in oxide and the formation of cracks are essentially related with two main microstructural changes occurring in transition to breakaway oxidation: formation of the flat GBs and the fine pores (about 3–10 nm in width).

Based on HR TEM observation, a schematic diagram is depicted in Fig. 5. In contrast to the oxide layer formed at a pre-breakaway transition with unclear and uneven GBs (Fig. 5a), breakaway oxidation transition led to the formation of enlarged grains having flat and clear GBs, resulting in enhanced oxygen diffusion into the oxide layer (Fig. 5b). This can be explained by the fact that GBs could be a short circuit associated with easier diffusion paths, as indicated by heavy arrows in Fig. 5b. That is, the GB with mismatch between adjacent crystal grains in the material's microstructure is a more open structure, allowing enhanced diffusion [15,16]. The relative diffusivities are $D_{\text{volume}} < D_{\text{grain boundary}} < D_{\text{surface}}$. Furthermore, micro-pores located at grain triple points and GBs are also open structures. For the crack formation during breakaway oxidation, micro-pores can increase the magnitude of the local stresses or cause a crack which appear to spread from the internal micro-pores to the GBs [17]. Thus, these micro-pores are considered to be the origin of the mechanical cracks in the oxide layer during breakaway oxidation. In addition, flat GBs in sample D are more favorable to crack propagation occurring during transition to breakaway oxidation than uneven GBs in sample A.

4. Conclusions

In conclusion, we demonstrated breakaway oxidation behavior and resulting microstructural changes of the oxide layer formed on the Zircaloy-4 tube at 1000 °C with a different oxidation time. Oxide layers with small grains showing unclear and uneven GBs were grown at relatively shorter oxidation time, whereas larger grains with flat GBs and micro-pores were observed in the oxide layer grown during transition to breakaway oxidation. The crystalline structure of ZrO_2 layers was characterized on an atomic scale by using HR TEM. Based on the microstructural changes affecting breakaway such as the shape of GBs and the formation of micro-pores, a mechanism was proposed to explain the process of breakaway oxidation transition.

Acknowledgement

This work was supported by Korean government's Ministry of Education, Science and Technology (MEST) through its Nuclear R&D Program.

References

[1] Nuclear Fuel Behaviour in Loss-of-Coolant Accident (LOCA) Conditions, State-of-the-Art-Report by the Nuclear Energy Agency. <http://www.nea.fr/html/pub/ret.cgi?div=NSD#6846>.
[2] G.R. Wallwork, C.J. Rosa, W.W. Smeltzer, Corros. Sci. 5 (1965) 113–120.
[3] R.A. Ploc, J. Nucl. Mater. 82 (1979) 411–418.
[4] T. Ahmed, L.H. Keys, J. Less Common Met. 39 (1975) 99–107.
[5] E. Tolksdorf, Corros. Sci. 14 (1974) 565–573.
[6] C. Roy, B. Burgess, Oxid. Met. 2 (1970) 235–261.
[7] C. Roy, G. David, J. Nucl. Mater. 37 (1970) 71–81.
[8] B. Cox, J. Nucl. Mater. 29 (1969) 50–66.
[9] J.H. Kim, M.H. Lee, B.K. Choi, Y.H. Jeong, J. Nucl. Mater. 362 (2007) 36–45.
[10] J.H. Baek, Y.H. Jeong, J. Nucl. Mater. 372 (2008) 152–159.
[11] C.V. Thompson, Annu. Rev. Mater. Sci. 30 (2000) 159–190.
[12] H.A. Porte, J.G. Schnizlein, R.C. Vogel, D.F. Fischer, J. Electrochem. Soc. 107 (1960) 506–512.
[13] S. Leistikow, G. Schanz, Nucl. Eng. Des. 103 (1987) 65–84.
[14] L.H. Keys, G. Beranger, P. Lacombe, J. Less Common Met. 14 (1968) 181–200.
[15] J.F. Shackelford, Introduction to Materials Science for Engineers, third ed., Macmillan Publishing Company, New York, 1985. pp. 115–132.
[16] A.E. Paladino, W.D. Kingery, J. Chem. Phys. 37 (1962) 957–962.
[17] L. Ewart, S. Suresh, J. Mater. Sci. 22 (1987) 1173–1192.